



Contents lists available at ScienceDirect



Electrochimica Acta

journal homepage: www.elsevier.com/locate/electacta

An experimental and theoretical approach on the effect of presence of oxygen in milled graphite as lithium storage material

C.B. Robledo^a, J.E. Thomas^b, G. Luque^a, E.P.M. Leiva^{a,1}, O. Cámara^a, D. Barraco^c, A. Visintin^{b,*1}

^a INFQ-C-CONICET-UNC. Departamento de Matemática y Física. Fac. de Ciencias Químicas. Universidad Nacional de Córdoba, Ciudad Universitaria, 5000 Córdoba, Argentina

^b Instituto de Investigaciones Fisicoquímicas Teóricas y Aplicadas (INIFTA), Fac. de Ciencias Exactas, UNLP, CCT La Plata-CONICET, C.C. 16, Suc. 4, CP 1900, La Plata, Argentina

^c Facultad de Matemática, Astronomía y Física, (IFEG), Universidad Nacional de Córdoba, Ciudad Universitaria, 5000 Córdoba, Argentina

ARTICLE INFO

Article history:

Received 14 December 2013

Received in revised form 24 May 2014

Accepted 25 May 2014

Available online xxx

ABSTRACT

The effect of milling time on the morphology of graphite is characterized by XRD, SEM, BET, FTIR and XPS and the electrochemical response of the resulting materials upon lithium-ion absorption is analyzed using different techniques. As milling time is increased, the particle size diminishes and the amount of oxygen content increases. Concomitantly, the capacity for lithium adsorption also increases because new adsorption sites become available due to more surface area and oxygen functional groups. These effects are interpreted using first-principles calculations, which show that the presence of oxygenated species promotes lithium adsorption at higher potentials. This capacity increase is probably not relevant for lithium-ion batteries since there is no intercalation process but rather an adsorption one, but may be of interest for supercapacitive applications. Diffusion coefficients of lithium for different graphite particle sizes are evaluated. The effects of diffusion, particle size and oxygen content are discussed.

© 2014 Elsevier Ltd. All rights reserved.

1. Introduction

The portable electronic boom of the last few years has been possible thanks to lithium-ion battery (LIB) technology, which was first presented in the market in 1991 by Sony, following the discovery of Goodenough's group, intercalation compounds [1]. Since then scientists have been putting a great effort into trying to understand all the electrode/electrolyte processes that occur simultaneously. In the last couple of years this interest has increased, not only in scientists but also in big automakers, since they are thought to be the best option to deliver great amounts of power to electric cars.

LIBs are composed of an anode and a cathode, separated by an electrolyte that isolates them electrically, but allows the transport of ionic species. Graphite is the material predominantly chosen nowadays for anodes of commercial LIBs, since it is a safer material than metallic lithium, it has a relatively high capacity and it is a

low-cost material. Because of its ability to intercalate both rapidly and reversibly one lithium atom per six carbon atoms, it has a theoretical capacity of 372 mAh g⁻¹ [2]. But in order to use them in very powerful electric cars, they should be improved to obtain higher energy and power densities and to achieve more charge and discharge cycles without capacity loss. To satisfy this it is necessary to achieve faster ion and electron transports in stable electrode materials [3]. Great efforts have been made to understand the lithium intercalation process in graphite [4–6] and the formation of the solid electrolyte interface (SEI) in the first cycles [7,8].

Mechanical milling is a simple and environmental friendly synthesis technique, very interesting from the industrial point of view, since it is scalable from the laboratory to the industry. The advantages are many. Upon increasing the mechanical energy, the appearance of cracks within the particles is favored; result being the breaking of particles and the creation of new fresh surface. In this way, the successive fracture of the particles will lead to a size decrease, which is therefore not unlimited since the increasing particles surface energy can outweigh the mechanical constraint energy, in which case the particles are going to form aggregates [9]. Tarascón and coworkers [10] observed that by increasing milling

* Corresponding author. Tel.: +54 221 4519199; fax: +54 221 4519199.

E-mail address: visintinarnaldo2@gmail.com (A. Visintin).

¹ ISE members.

time up to 80 h, both the reversible and irreversible capacity values of graphite and coke increased up to 708 mAh g⁻¹ and 328 mAh g⁻¹, respectively, and they attributed this additional reversible capacity to the adsorption of lithium ions on the carbon surface. Wang et al. [11] characterized ball-milled graphite up to 150 h and reported a reversible capacity of 700 mAh g⁻¹, which is about twice that of pristine graphite. The additional reversible capacity was attributed to additional Li doping at vacancies, microcavities and voids.

A number of interesting questions appear on the basis of the previous reports. What happens to the carbon surface? What kind of interaction does the lithium ion have with these surfaces? Is the change in the storage capacity of these structures only due to size effects and appearance of defects, or is there any other modification of the material taking place upon milling in air? To gain understanding on such processes, more investigation at the atomistic level is required, complemented by experimental results. With this purpose, we investigated the effect of ball milling of graphite flakes under air atmosphere on its electrochemical response as anode for lithium-ion batteries. We focused mainly on the intrinsic lithium storage mechanism related to the surface chemistry present in the active materials synthesized. We complemented the experimental results with first-principles calculations. The novelty of this work is the demonstration by experimental and theoretical tools the role that the presence of oxygen has on the lithium storage mechanism in graphite. Furthermore, it is shown that the increment of capacity for lithium storage in these materials is not only produced by the increment of surface area due to ball milling.

2. Experimental

2.1. Samples and physical characterization

The different graphite samples of the present work were prepared by ball milling commercially available graphite flakes (Sigma Aldrich, surface area < 5 m²/g) under an air atmosphere. The experiment was carried out in a planetary ball mill (Fritsch PULVERISETTE 7 premium line) with hard metal tungsten carbide grinding bowl and zirconium oxide balls (diameter: 10 mm). The ratio of the ball mass to powder was 22:1. The milling was carried out at a speed of 400 rpm and it was programmed so that every 30 min of milling there would be a pause of 30 min (to prevent excessive heating). This was done until the total milling time was found to be 5, 10, 15 and 20 h. The samples were named MG5, MG10, MG15 and MG20, in agreement with the milling time (MG stands for milled graphite).

The structural changes of the ball-milled graphite samples were characterized using X-ray powder diffraction with Cu K α ($\lambda=1.5418\text{ \AA}$) radiation, measured on a PANalytical X'Pert PRO diffractometer. The microstructure of the samples was examined by scanning electron microscopy (SEM). The Brunauer-Emmett-Teller (BET) surface area was obtained by a single-point method, measured by ChemiSorb 2720. For Fourier transform infrared measurements (FTIR) the different ball-milled samples were mixed with KBr (spectroscopy grade) in 1:100 proportions and crushed in an agate mortar. The mixture was compressed to a semitransparent disk by applying a pressure of 8 tons for 30 sec. The FTIR spectra over the wavelength range of 3500–500 cm⁻¹ were recorded using a FTIR spectrometer (BRUKER IFS66 v). X-ray photoelectron spectroscopy (XPS) was performed in situ using a VG Microtech ESCA spectrometer with a non-monochromatic Al K α radiation (300 W, 15 kV, $h\nu=1486.6\text{ eV}$) as the excitation source combined with a VG-100-AX hemispherical analyzer operating at 25 eV pass energy. The instrumental resolution was 0.1 eV. Samples were outgassed at room temperature in the preparation chamber (10^{-6} Torr), until constant pressure was achieved and then introduced to the analysis chamber (10^{-9} Torr) for recording the spectra.

2.2. Electrochemical measurements

MG electrodes were prepared by coating a mixture of active material, polyvinylidenefluoride (PVDF) binder and conductive carbon Black (Timcal Super P) in a weight ratio 80:10:10, dispersed in N-methyl-2-pyrrolidone, onto a 9 mm thick copper foil. All the electrodes prepared with the different MG samples were pressed (5 ton/cm²) and dried at 80 °C overnight under vacuum before introducing them in a glovebox (Mbraun, filled by Ar atmosphere with a concentration of O₂ and H₂O less than 1 ppm). The coated MG electrodes were punched into 6 mm diameter disks. Three-electrode cells were assembled inside a glovebox, with metallic lithium as reference and counter electrodes and an electrolyte-soaked fiberglass separator. The electrolyte consisted of ethylene carbonate (EC) and dimethyl-carbonate (DMC) mixture (1:1 by mass) containing 1 M LiPF₆ salt. The samples milled for 5 h (MG5) were discarded for electrochemical measurements, due to the relative big size of the graphite flakes. This prevented the formation of a stable coat onto the copper foil.

Initially, ten charge-discharge cycles were performed at a current of C/2 with cut off potentials of 0 and 1.5 V vs. Li⁺/Li⁰, which was the reference electrode selected. Cyclic voltammetry (CV) was performed on the electrodes at three different speeds (0.1, 1 and 10 mV/s) between the same window potential as the previous experiment. After the CV experiments, electrochemical impedance spectroscopy (EIS) measurements were made at three different points of the discharge curve: 100%, 50% and 0% of SOC¹ (previous stabilization at open circuit potential, E₀, for 15 min). The EIS spectra were recorded at E₀, in the 100 kHz–5 mHz frequency range, with a 5 mV amplitude. Finally, rate capability experiments were performed with the same cut off potentials and the charge current value reported above, but the discharge currents used were C/5, C/2, C, 2 C, 5 C and 10 C.

3. Model and Computation

DFT calculations were performed employing the SIESTA computer code [12,13]. A localized basis set composed of double-plus polarization was used. The basis functions were numerical atomic orbitals (NAOs), the solutions of the Kohn-Sham Hamiltonian for the isolated pseudoatoms. Exchange and correlation effects were described using a generalized gradient approximation (GGA), within the Perdew-Burke-Ernzerhof (PBE) functional [14]. The atomic cores were replaced by norm conserving pseudopotentials [15] in their fully separable form [16]. In the pseudopotential description of the atoms, only valence electronic states were considered. The value of the confinement parameters were defined variationally applying the simplex method [17]. The cut off of the grid for real-space integrals [12] yielded converged results for all the systems studied here using a value of 150 Ry. All calculations were performed with spin polarization (sp).

We decided to study the analysis of the effect of defects and oxygen content in graphite, introduced in the milling process, through the calculations with configurations of a single graphene layer since it requires less computational effort. For the sake of comparison between configurations, it is expected that the relative differences in energy are similar and that conclusions can be extrapolated to graphite.

The graphene sheet was represented by a 60 carbon atom basis, arranged in a honeycomb pattern. The unit cell was tetragonal $12.31\text{ \AA} \times 12.80\text{ \AA} \times 20\text{ \AA}$ with periodic boundary conditions in x, y, z directions imposed in order to represent an infinite surface.

¹ SOC stands for State of Charge.

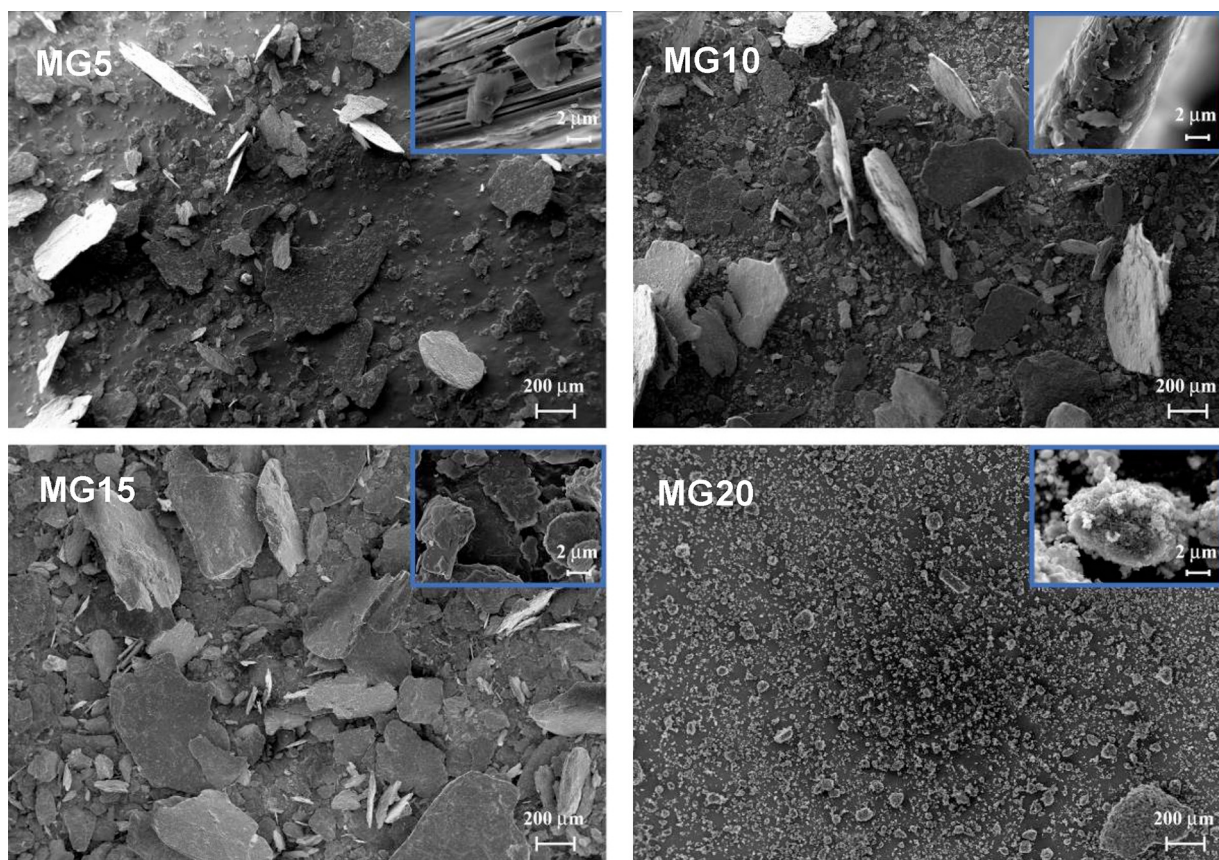


Fig. 1. Scanning electron microscopy images of milled graphite samples. In the smaller image located in the upper right corner of each SEM image, a zoom with scale 2 μm is shown.

For the analysis of systems with oxygenated groups at the borders of graphene, the unit cell employed was tetragonal $24.63 \text{ \AA} \times 12.80 \text{ \AA} \times 20 \text{ \AA}$, with periodic boundary conditions only applied in the y direction, to represent the borders. The cohesive energy of lithium was calculated minimizing the energy of a BCC unit cell, using the isolated atoms as a reference. The binding energy, E_b , of a lithium atom adsorbed on different structures was calculated from:

$$E_b = E_{(Gr-Li)} - E_{(Gr)} - E_{(Li)}, \quad (1)$$

where, $E_{(Gr-Li)}$ is the energy of the graphenic system containing lithium, $E_{(Gr)}$ is the energy of the system without lithium and $E_{(Li)}$ is the energy of an isolated lithium atom. $E_{(Gr)}$ may correspond to the system with or without defects or in the presence of oxygenated species.

All energies were obtained with the conjugate gradient (CG) technique [17], minimizing the energy of the system from an initial configuration with respect to the atomic coordinates.

4. Results and Discussion

4.1. Structural Characterization

Morphologies of the ball-milled graphite samples, obtained using SEM, are shown in Fig. 1. As the milling time increases, the size of the graphite flakes decreases. For MG20, agglomerates of 5 to 10 μm composed of smaller nano-sized particles are observed. It is also found that with an increase in the milling time, there is a loss in the laminar structure of graphite, until a porous material is formed. It has been previously reported that upon continuous milling, graphite particles reach a critical size threshold beyond which the increasing surface energy favors the merging of single

particles, forming agglomerates. Such agglomeration is expected to increase the particle size and thereby decrease the effective surface area [9].

The X-ray diffraction curves of the MG samples are shown in Fig. 2. As the milling time is increased, the XRD curves show a significant decrease in the intensity and broadening of the [002] Bragg peak at approximately 26.5° , indicating increased disorder of the graphite structure [10]. The value of FWHM increases from 0.13 in MG5 to 0.37 in MG10, and finally reaches 2.84 in MG20. Hence, it can be concluded that as milling time increases, the crystallinity of graphite decreases and it is transformed into a more amorphous

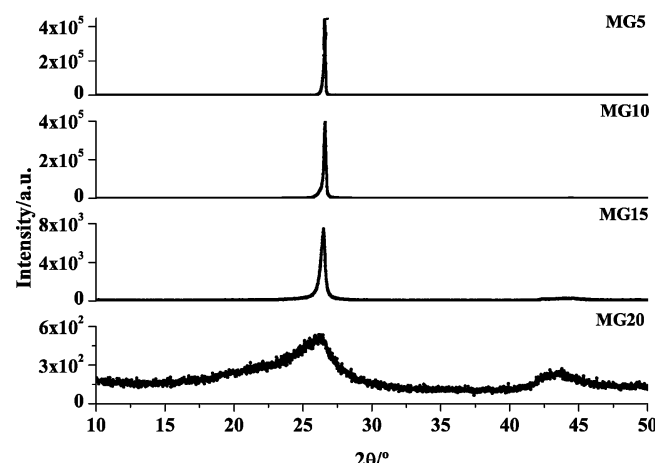


Fig. 2. X-ray diffraction curves of ball-milled graphite samples. The peak at approximately 26° corresponds to the diffraction of the plane 002.

Table 1

Surface area data obtained from the BET measurements for commercial graphite flakes and two of the milled samples.

Sample	Surface area [m ² /g]
Graphite	0.82
MG10	13.57
MG20	462.80

material. These results are in agreement with the SEM images that show a loss in the laminar structure of graphite as milling time is increased.

The values of surface area of the different samples, as obtained from BET experiments, are listed in **Table 1**. It is observed that as grinding time increases, the surface area also increases. This also agrees with the results from SEM, where it is observed that particle size decreases with an increase in milling time, leading to a greater surface area. FTIR spectra of the different samples are shown in **Fig. 3**. The unmilled graphite sample has a very weak band at 1005 cm⁻¹, which corresponds to the stretching of the C-O-C bonds in epoxy groups. So, commercial graphite has very few oxygen functional groups. This band is also present in the milled samples, in addition to a band at 1232 cm⁻¹ that corresponds to the vibration of C-O bonds in alcohols, esters, carboxylic acids, and

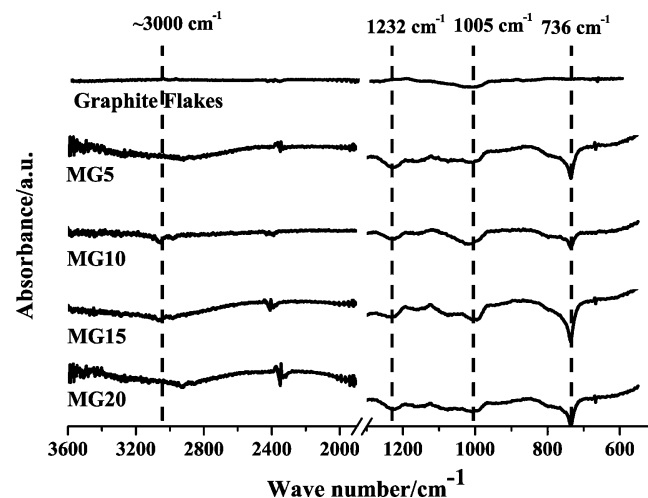


Fig. 3. FTIR spectra of the graphitic samples obtained after different milling times. The spectrum of unmilled graphite flakes is shown for comparison.

ethers. Also a band at approximately 3000 cm⁻¹ appears in the milled samples, corresponding to the –OH vibration mode in carboxylic groups. The strong band appearing at 736 cm⁻¹, is usually assigned to the “rocking” mode vibration of dangling C-H bonds that

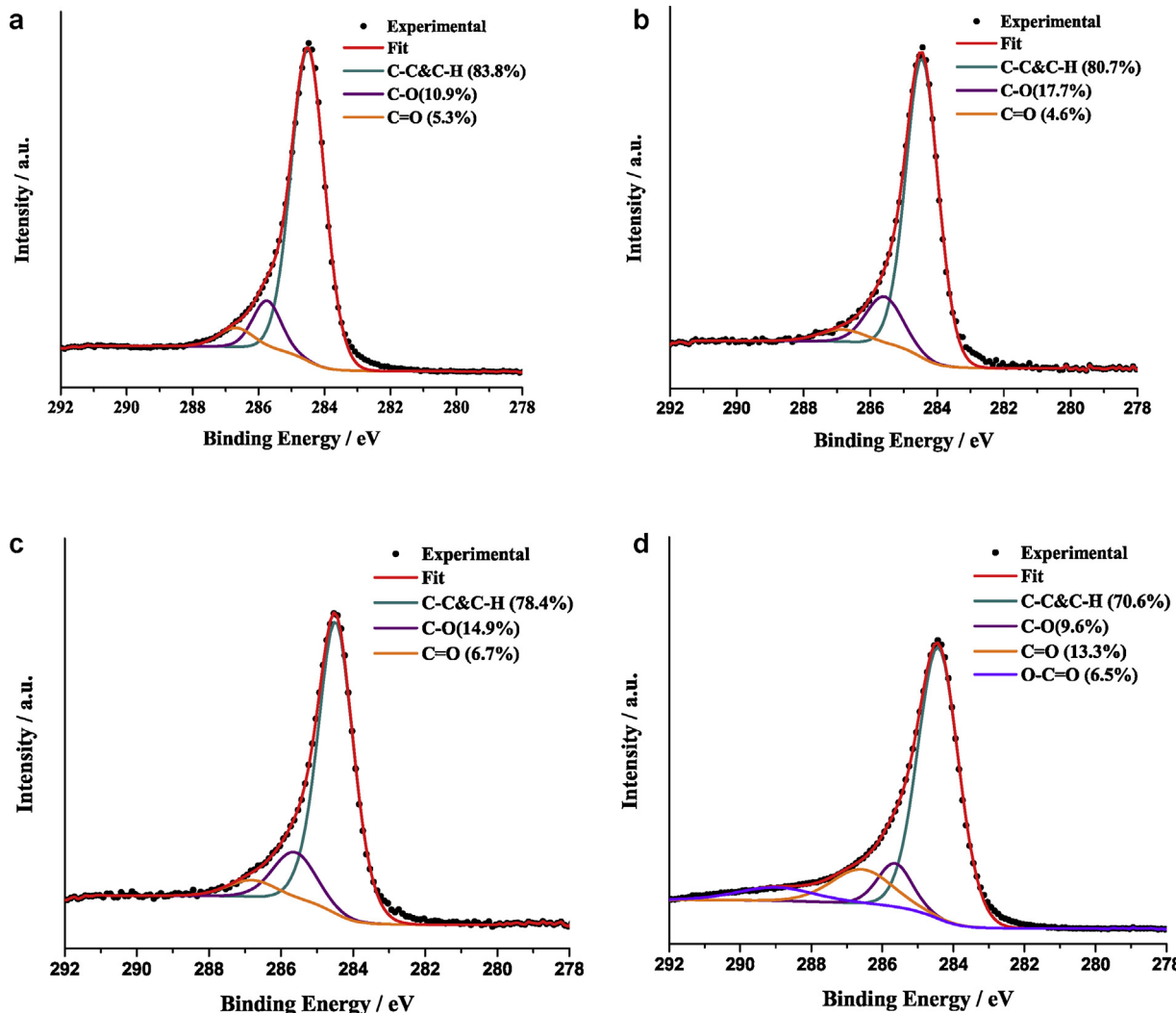


Fig. 4. C1S XPS spectra of the different samples of ball-milled graphite flakes. (a) Commercial graphite flakes, (b) MG10, (c) MG15 and (d) MG20.

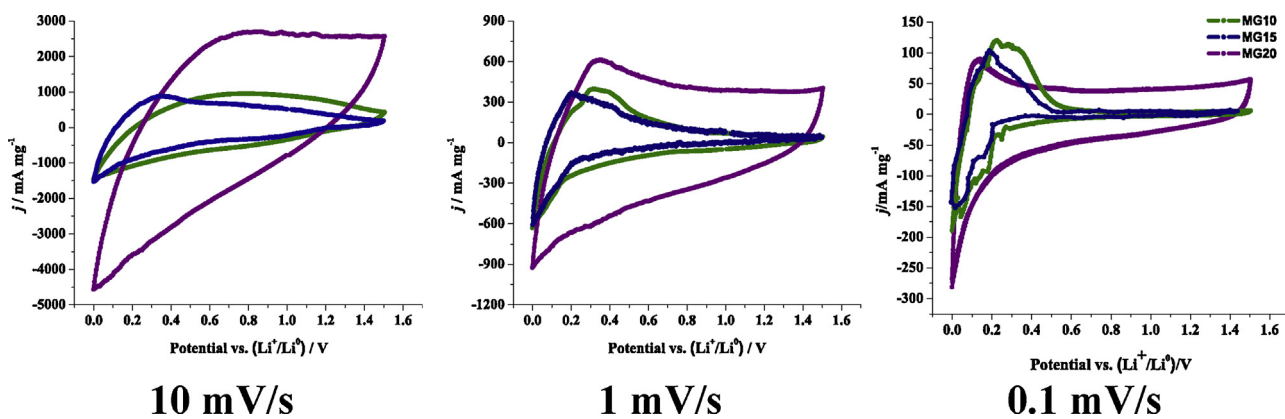


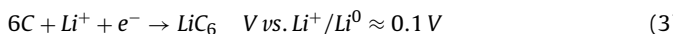
Fig. 5. Cyclic voltammetry curves obtained with the different samples of ball-milled graphite flakes at three different scan rates. Purple: MG20; Blue: MG15; Green: MG10.

appear in the milling process. Thus, we can state that the milling process in air atmosphere introduces oxygen functional groups into the graphite samples. To get quantitative information about the occurrence of these groups, we obtained XPS spectra from these samples (see Fig. 4). It is found that as milling time is increased the amount of oxygen functional groups increases. Concomitantly, the quantity of C-C and C-H bonds decreases from 83.8% in unmilled graphite to 70.6% in the sample milled for 20 h. In the particular case of the sample milled for 20 h, -COOH and C-O species, which were absent in other cases, appeared. These species are expected to occur at the edges of the graphite planes, thus providing highly coordinated adsorption sites for lithium species.

4.2. Electrochemical characterization

Fig. 5 shows cyclic voltammetry experiments at three different scanning rates for the MG samples. As the scanning rate decreases, the peaks corresponding to the intercalation mechanism of lithium ions into graphite start to appear. The difference between the three samples is that for the more amorphous material (MG20), only one peak is observed. Meanwhile, in MG10 and MG15 more than one intercalation peak appear. This indicates the formation of different phases in the samples as lithium ions are intercalated.

The intercalation peaks appear more clearly and sharpen in the voltammogram recorded at 0.1 mV/s because the diffusion process of the lithium ion into the particles of graphite is a very slow process. As has been previously reported, the different Li^+ intercalation processes occur below 0.25 V [18]. These processes can be synthesized as follows in equations (2) and (3):



The charge/discharge curves for the 10th cycle are shown in Fig. 6. Upon charge or discharge, the curves for MG20 do not present a significant plateau in the potential, and this electrode has the highest reversible capacity of the three electrodes (approximately 250 mAh g^{-1}). This could be due to the presence of more adsorption sites for lithium ions because of the higher specific surface area of MG20 in comparison with the other samples. MG10 had a reversible capacity of approximately 100 mAh g^{-1} and MG15, 120 mAh g^{-1} . The capacity values here reported are lower than those of commercial Timcal's TIMREX S-family of graphite electrochemically active for commercial batteries [19], because our particles are not highly crystalline as those commercially available, due to the milling process. Also, since we start from a raw material, as it is graphite flakes, the particles size of the samples MG15 and MG10 are bigger than the optimum size (less than $10 \mu\text{m}$). For the purpose

of analyzing the effect of the presence of oxygen functional groups on the surface of the active material, this matter is not a problem.

Impedance spectra obtained for the MG samples for three different states of charge (SOC) are presented in Fig. 7. In the three states, the Nyquist plots, at high frequencies (100 kHz–10 kHz), exhibit a slope close to 45° , a typical response of porous electrodes. Then, in the intermediate range of frequencies (10 kHz–100 Hz), there is a depressed semicircle or a sum of two semicircles. Finally, at low frequencies ($< 100 \text{ Hz}$) there is a typical 45° slope line representing a Warburg impedance related to finite diffusion (Li^+ intercalation into graphite).

To obtain electrochemical parameters of the lithium storage process, such as diffusion coefficient (D_{Li^+}), electroactive area (A_{ea}) of the electrode and exchange current (j_0), we used an equivalent circuit to adjust the impedance results for/to 50% SOC. We used a simplified version of the most commonly used circuit in the literature for this type of material [20], where we neglect the resistance of the passivating film, since it is very small compared with the resistance of the charge transfer. The equivalent circuit is represented in Fig. 8, where R_{int} corresponds to the resistance of the electrolyte, R_{ct} is the charge transfer resistance, CPE is a constant phase element, which corresponds to the capacity of the film, and $W1$ is Warburg impedance.

To obtain the electroactive area of the electrodes it was necessary to calculate the pseudocapacitance of the CPE. The pseudocapacitance is defined according to:

$$C_{pseudo} = Y_0^{\frac{1}{n}} R^{\left(\frac{1}{n}-1\right)} \quad (4)$$

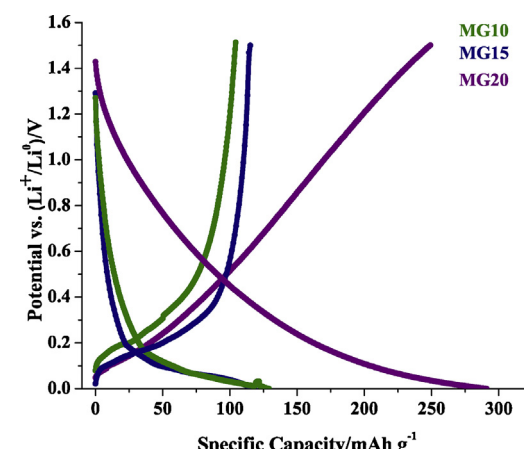


Fig. 6. Comparison of galvanostatic charge and discharge curves of the three electrodes tested, at the 10th cycle between 0 V and 1.5 V (vs. Li^+/Li^0) at a current of C/2.

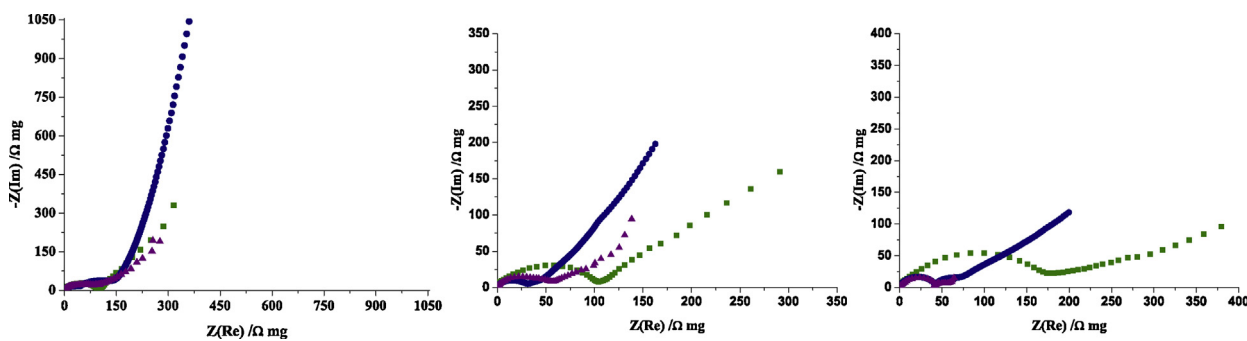


Fig. 7. Nyquist electrochemical impedance spectroscopy diagrams for three states of charge of the samples studied. From left to right: 0, 50 and 100% SOC.

Table 2

Electrochemical parameters as obtained by the equivalent circuit fit of EIS for the three electrodes at 50% SOC: specific electroactive area, S_{ea} , current density, j_0 , Warburg coefficient, σ and lithium diffusion coefficient, D .

	S_{ea} [cm ² /g]	j_0 [mA/cm ²]	σ [Ω/\sqrt{s}]	D [cm ² /s]
MG10	56	4.19	14.7	3.2×10^{-10}
MG15	275	2.85	12.3	2.4×10^{-11}
MG20	396	1.08	33.4	1.6×10^{-11}

where Y_0 is the admittance corresponding to the CPE for $\omega = 1$ rad/s, n is the exponent in the expression of the impedance for the CPE ($0 \leq n \leq 1$) and R is the sum of the R_{ct} and the resistance corresponding to the Warburg impedance, which is in parallel with CPE ($R = R_{ct} + W1 - R$). The pseudocapacitance is related to the electroactive area according to:

$$C_{pseudo} = C_{dl} A_{ea} \quad (5)$$

where C_{dl} is constant and equal to 5×10^{-5} F/cm² [21].

To compare the three electrodes, the calculated values of specific electroactive area $S_{ea} = A_{ea}/m$ (m is the active mass of the electrode) are listed in Table 2, together with the other results from the impedance fit. As milling time is increased, the value of S_{ea} is also increased/also increases. We relate this effect to the occurrence of smaller particles due to the milling process.

The exchange current is related to the charge transfer and the electroactive area through equation (6):

$$j_0 = \frac{RT}{nR_{tc}FA_{ea}}, \quad (6)$$

where R is the ideal gas constant, 8.314 J/molK, T is the temperature of the experiment, 298 K, n in this case is the number of electrons involved in the electrochemical reaction, which is 1, and F is the Faraday constant, 96485 C/mol. The results are listed in Table 2. It is observed that as milling time is increased, the exchange current decreases. Assuming that the exchange current density is proportional to the density of states of the carbonaceous anode at the Fermi level [22], say $\rho_C(E_F)$,

$$j_0 \propto \rho_C(E_F), \quad (7)$$

The latter experimental observation can be related to the crystallinity of the samples. When graphite is milled to generate particles at the nanoscale, the laminar structure is broken and the

crystallinity decreases, as can be seen from XRD experiments. On the other hand, the decrease in j_0 indicates that electron exchange with graphite is slowed down as the particle size decreases. Density functional calculation of the electronic structure of graphite shows that it is semimetallic [23]. However, Koivusaari et al. have shown that C amorphous networks with a high sp_3 character present an increased band gap, that is, a decreased density of states at the Fermi level [24]. Thus, the present observation of a decreased exchange current density may be correlated with the progressive amorphization of the C structure with the concomitant decrease of its density of states at the Fermi level.

To calculate the lithium ion diffusion coefficient from the impedance results, first it was necessary to estimate the Warburg coefficient, σ , from the linear part of the Nyquist plot (frequencies higher than $2/W1-T$). We calculated σ as the average of the two slopes of the graphic representations of Z_{re} vs. $\omega^{-1/2}$ y Z_{im} vs. $\omega^{-1/2}$. The results are shown in Table 2. The Warburg coefficient is related to the diffusion coefficient of Li^+ through equation (8) [25]:

$$\sigma = \left[\frac{RT}{\sqrt{2}n^2F^2AC_{Li^+}} \right] \frac{1}{\sqrt{D_{Li^+}}}, \quad (8)$$

where R is the ideal gas constant, T is the absolute temperature, n the number of transferred electrons in the electrochemical reaction, A the geometrical electrode area, and C the concentration of Li^+ intercalated. Equation (8) can be written as equation (9) to obtain the lithium ion diffusion coefficient:

$$D_{Li^+} = \frac{R^2T^2}{2A^2n^4F^4C_{Li^+}^2\sigma^2}. \quad (9)$$

The value of C_{Li^+} (mol/cm³) is calculated from the molar volume of milled graphite for a 50% SOC. The calculated values of the diffusion coefficient (see Table 2) are in the same order as those reported in the literature [5,26]. Previous reports we have found are related to the dependence of the diffusion coefficient on the variation in temperature [27] or on the amount of lithium ions intercalated [5]-[20], but to the best of our knowledge D_{Li^+} for electrodes with different particle sizes of the active material have not been previously reported. To understand how the milling time of graphite samples affects the value of the diffusion coefficient of Li^+ , we compared D_{Li^+} in the three MG samples for the same state of charge (50% SOC). As milling time is increased and the size of the graphite flakes gets smaller, the diffusion coefficient of the charged species of lithium decreases. This can be related to the crystallinity decrease of the successive milled samples. By mechanical grinding, the laminar structure of graphite is reduced and thus, the number of diffusive pathways for ion Li^+ is smaller (because the ions diffuse in the direction parallel to the graphene layers).

Rate capability experiments were carried out to evaluate the response of the materials under different discharge currents. The plot of the percentage of maximum discharge capacity (Q_{max}) vs.

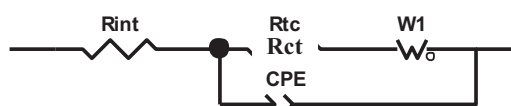


Fig. 8. Equivalent circuit used to fit the impedance results for the milled graphite electrodes.

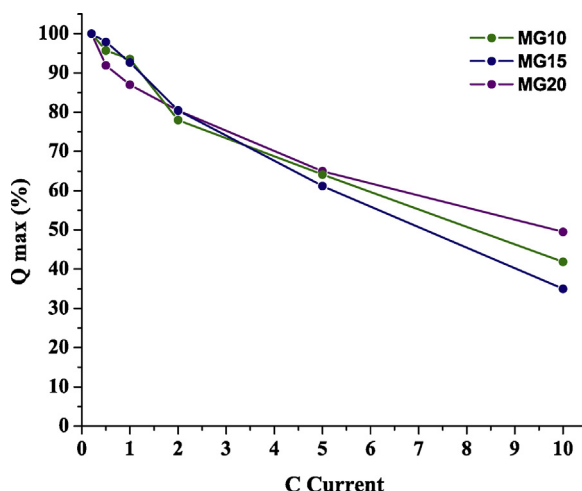


Fig. 9. Rate capability experiment for the three electrodes tested.

discharge current, expressed in terms of C current is shown in Fig. 9. The three electrodes have a similar behavior until 10 C. This could be because of the morphology and size of the particles of each electrode and the intrinsic process of intercalation/deintercalation. We suppose that since MG20 has the smallest graphite particles, the majority of the lithium ions are stored on the surface of the active material and not inside it. The XPS analysis indicates that -COOH or C-OH species may appear at the edges of these small particles, providing new adsorption sites for lithium. This could be the reason why they discharge more rapidly at higher discharge currents, although they exhibit the lowest exchange current density.

We now present the results of first-principles calculations, where we study the interaction of the lithium ion with different adsorption sites. The binding energy of a single lithium ion with a graphene sheet was calculated to be -0.87 eV. This is a weak interaction energy as compared to the cohesive energy of lithium (-1.40 eV) calculated with the same methodology, indicating that the deposition of lithium on such a surface should take place at lower potential than bulk lithium deposition. In fact, the previous results indicate that the energy change of the following reaction:



is $\Delta U = 0.53$ eV. Neglecting entropic contributions, we can thus write $0.53\text{ eV} = -e_0 \Delta E^0$, where ΔE^0 is the equilibrium potential of an electrode with Li adsorbed on graphene in the Li^+ scale. Thus, we conclude that lithium deposition on a graphenic surface should

take place at -0.53 V vs. Li^0/Li^+ . The present results are in agreement with similar calculations from the literature [28]. The situation of Li deposition on graphite should not be very different, since the adatom interacts essentially with the surface layer. Thus, the previous argument shows that straightforward increase of the surface area should not lead to a stronger binding of lithium to the active material or what is equivalent, to Li deposition at higher potentials than those involved in lithium insertion in regular graphite. Therefore, Li storage at higher potentials, as found in the present experiments, must be explained on different grounds.

It is well known that severe plastic deformations and defects are introduced by ball-milling in graphite [29]. Thus, one possibility is that lithium binds stronger to defects. To consider this point, lithium adsorption on two types of defects common on graphene were studied, as shown in Fig. 10. The first is a vacancy defect (shown in Fig. 10a), which occurs when a C atom is missing from the 6 carbon ring present in graphite. The second is a Stone-Wales defect (shown in Fig. 10b), which is one of the most common types of stable defects on carbon nanotubes and graphene that appear due to a defective reconstruction of holes on the surface where a C-C bond is formed by 90° rotation about its center, which converts a group of four adjacent hexagonal rings into a (5,7,7,5) ring cluster [30]. A vacancy defect favors Li adsorption with a binding energy of -2.37 eV , while the sheet with a Stone-Wales binds Li with a -1.98 eV adsorption energy. These values are considerably larger in absolute value than the 0.87 eV observed for a surface without defects. Therefore we can state that binding of Li on these defects is more favorable than binding to a perfect graphite surface.

Another possibility that must be considered to explain lithium storage at relatively high potentials is a stronger bond to the surface induced by the presence of oxygen functional groups. Since it was evident from XPS spectra the presence of C-OH, C=O and -COOH species in the milled samples, we considered in our calculations the interaction of a lithium atom with the oxidized graphenic surfaces shown in Fig. 11. In this configuration all the oxygen functional groups were introduced at the border of the graphene sheet, as expected to appear in the milling process. In this case a very strong binding energy was obtained, -3.41 eV . This result shows that lithium storage may occur in these structures at potentials as high as 2 V .

Previous reports have attributed the incremental capacity of carbon based anodes to the adsorption of lithium in the vacancies, microcavities, voids and defects [11,31]. However, the present calculations show that oxygen functional groups may offer a stronger interaction with lithium than those provided by defects.

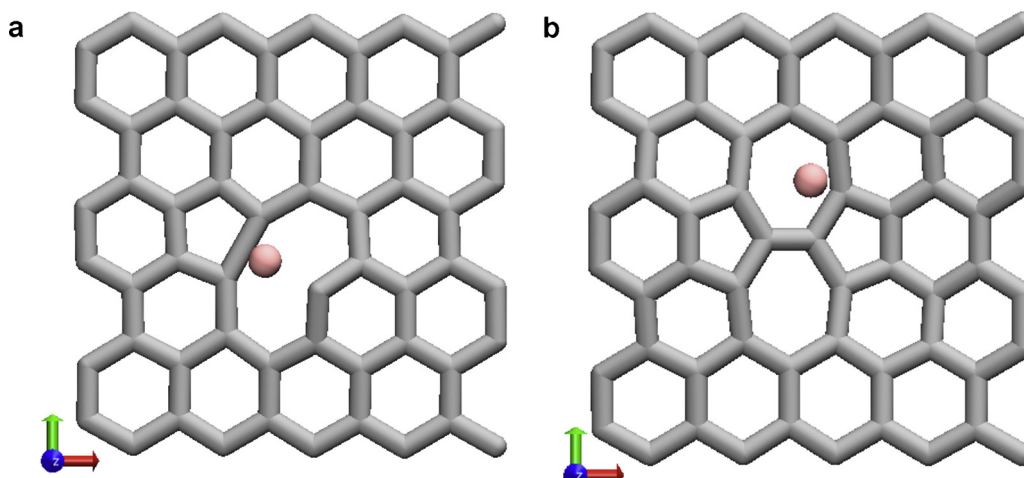


Fig. 10. Optimized structures of a lithium atom adsorbed on a graphene sheet with defects: a) vacancy defect and b) Stone-Wales defect. Grey: C; Pink: Li.

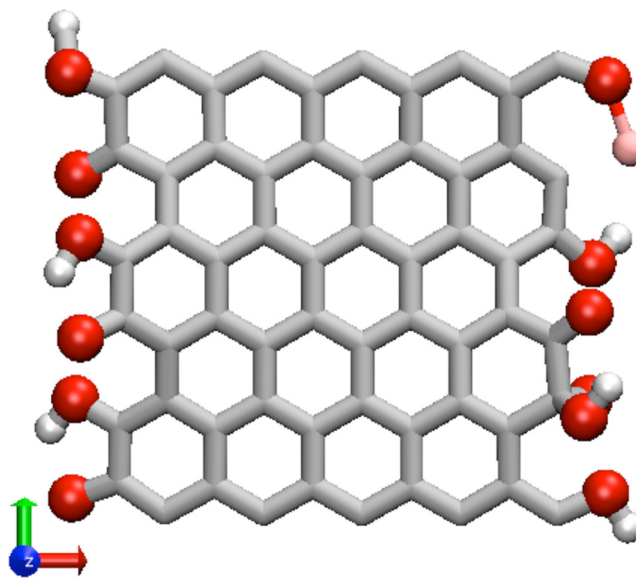


Fig. 11. Optimized structure of a lithium atom adsorbed on a graphene sheet with oxygen functional groups at the borders. Grey: C; Red: O; White: H; Pink: Li.

5. Conclusions

We presented a thorough morphological and electrochemical characterization of ball milled graphite flakes as anodes for lithium ion batteries. As the grinding time is increased, the surface area value of graphite flakes is increased and the particle size decreased. The XPS results indicate that the oxygen content of the sample also increases with milling time. The present results show that the amount of lithium intercalated and are strongly dependent not only on the graphite particle size, but also on the oxygen content present in the samples. As milling time is increased and the size of the graphite flakes gets smaller, the laminar structure is broken and the crystallinity decreases, the diffusion coefficient of the charged species of lithium decreases as well. All the samples show a similar behavior and good rate capability up to 10 C.

The charge/discharge curves for MG20 present a capacity of approximately 250 mAh/g for low current discharge, MG10 had a reversible capacity of approximately 100 mAh/g and MG15, 120 mAh/g. We attribute the occurrence of more adsorption sites for lithium ions to the presence of oxygen-containing species that are incorporated during the milling process. These oxygenated species bind lithium to the surface stronger than pristine graphite and even stronger than defective surfaces, playing a key role in promoting lithium adsorption at more positive potentials.

Acknowledgments

This work was supported by PID 2011-0070, Program BID (PICT-2011-0754, 2012-2324), and SeCyT of the Universidad Nacional de Córdoba, Argentina. C. B. Robledo wishes to thank CONICET for the doctoral fellowship. This work was performed at INIFTA, Universidad Nacional de La Plata, Argentina, and INFIQC, Universidad Nacional de Córdoba, Argentina.

References

- [1] Z. Xiong, Y. Yun, H.-J. Jin, Applications of Carbon Nanotubes for Lithium Ion Battery Anodes, *Materials (Basel.)* 6 (2013) 1138–1158.
- [2] P.B. Balbuena, Y. Wang, *Lithium-Ion Batteries: Solid-electrolyte Interphase*, Imperial College Press, London, England, 2004.
- [3] Y.J. Mai, J.P. Tu, C.D. Gu, X.L. Wang, Graphene anchored with nickel nanoparticles as a high-performance anode material for lithium ion batteries, *J. Power Sources* 209 (2012) 1–6.
- [4] H. Shi, J. Barker, M. Saidi, R. Koksbang, L. Morris, Graphite structure and lithium intercalation, *J. Power Sources* 68 (1997) 291–295.
- [5] T. Piao, S. Park, C. Doh, S. Moon, Intercalation of lithium ions into graphite electrodes studied by AC impedance measurements, *J. Electrochem. Soc.* 146 (1999) 2794–2798.
- [6] E. Barsovskov, J. Kim, C. Yoon, H. Lee, Kinetics of lithium intercalation into carbon anodes: in situ impedance investigation of thickness and potential dependence, *Solid State Ionics* 116 (1999) 249–261.
- [7] M. Holzapfel, A. Martinent, F. Alloin, B. Le Gorrec, R. Yazami, C. Montella, First lithiation and charge/discharge cycles of graphite materials, investigated by electrochemical impedance spectroscopy, *J. Electroanal. Chem.* 546 (2003) 41–50.
- [8] M. Nie, D. Chalasani, D.P. Abraham, Y. Chen, A. Bose, B.L. Lucht, Lithium Ion Battery Graphite Solid Electrolyte Interphase Revealed by Microscopy and Spectroscopy, *J. Phys. Chem. C* 117 (2013) 1257–1267.
- [9] J.-M. Tarascon, M. Moretto, J. Saint, L. Aymard, R. Janot, On the benefits of ball milling within the field of rechargeable Li-based batteries, *Comptes Rendus Chim.* 8 (2005) 17–26.
- [10] F. Disma, L. Aymard, L. Dupont, J.-M. Tarascon, Effect of mechanical grinding on the lithium intercalation process in graphites and soft carbons, *J. Electrochem. Soc.* 143 (1996) 3959–3972.
- [11] C.S. Wang, G.T. Wu, W.Z. Li, Lithium insertion in ball-milled graphite, *J. Power Sources* 76 (1998) 1–10.
- [12] P. Ordejón, E. Artacho, J.M. Soler, Self-consistent order-N density-functional calculations for very large systems, *Phys. Rev. B* 53 (1996) R10441–R10444.
- [13] J.M. Soler, E. Artacho, J.D. Gale, A. García, J. Junquera, P. Ordejón, et al., The SIESTA method for ab initio order- N materials simulation, *J. Phys. Condens. Matter.* 14 (2002) 2745.
- [14] J. Perdew, K. Burke, M. Ernzerhof, Generalized Gradient Approximation Made Simple, *Phys. Rev. Lett.* 77 (1996) 3865–3868.
- [15] N. Troullier, J.L. Martins, Efficient pseudopotentials for plane-wave calculations, *Phys. Rev. B* 43 (1991) 1993–2006.
- [16] L. Kleinman, D. Bylander, Efficacious Form for Model Pseudopotentials, *Phys. Rev. Lett.* 48 (1982) 1425–1428.
- [17] W.T.V.W.H. Press, B.P. Flannery, S.A. Teukolsky, Numerical Recipes, *The Art of Scientific Computing*, Cambridge University Press, Cambridge, 1986.
- [18] H. He, C. Huang, C.-W. Luo, J.-J. Liu, Z.-S. Chao, Dynamic study of Li intercalation into graphite by in situ high energy synchrotron XRD, *Electrochim. Acta.* 92 (2013) 148–152.
- [19] Brochure TIMREX S-family Technical Data, <http://www.timcal.com/Scopi/Group/Timcal/timcal.nsf/pagesref/SCMM-7EVSQL?OpenDocument&lang=en>, last date accessed: 15/05/2014.
- [20] N. Takami, A. Satoh, M. Hara, T. Ohsaki, Structural and kinetic characterization of lithium intercalation into carbon anodes for secondary lithium batteries, *J. Electrochem. Soc.* 142 (1995) 371–378.
- [21] F. Béguin, E. Frąckowiak, *Carbons for Electrochemical Energy Storage and Conversion Systems*, CRC Press, Boca Raton, FL, 2010.
- [22] W. Schmickler, C. Widrig, The investigation of redox reactions with a scanning tunneling microscope: Experimental and theoretical aspects, *J. Electroanal. Chem.* 336 (1992) 213–221.
- [23] N. Ooi, A. Raikar, J.B. Adams, Density functional study of graphite bulk and surface properties, *Carbon* 44 (2006) 231–242.
- [24] K.J. Koivusaari, T.T. Rantala, J. Levoska, S. Leppävuori, Surface electronic density of states of tetrahedral amorphous carbon investigated by scanning tunneling spectroscopy and ab initio calculations, *Appl. Phys. Lett.* 76 (2000) 2794.
- [25] H. Liu, C. Li, H.P. Zhang, L.J. Fu, Y.P. Wu, H.Q. Wu, Kinetic study on LiFePO₄/C nanocomposites synthesized by solid state technique, *J. Power Sources* 159 (2006) 717–720.
- [26] M.D. Levi, D. Aurbach, Diffusion Coefficients of Lithium Ions during Intercalation into Graphite Derived from the Simultaneous Measurements and Modeling of Electrochemical Impedance and Potentiostatic Intermittent Titration Characteristics of Thin Graphite Electrodes, *J. Phys. Chem. B* 5647 (1997) 4641–4647.
- [27] G. Zhao, Z. Wei, N. Zhang, K. Sun, Enhanced low temperature performances of expanded commercial mesocarbon microbeads (MCMB) as lithium ion battery anodes, *Mater. Lett.* 89 (2012) 243–246.
- [28] E. Lee, K. a Persson, Li absorption and intercalation in single layer graphene and few layer graphene by first principles., *Nano Lett.* 12 (2012) 4624–8.
- [29] T. Xing, L.H. Li, L. Hou, X. Hu, S. Zhou, R. Peter, et al., Disorder in ball-milled graphite revealed by Raman spectroscopy, *Carbon* 57 (2013) 515–519.
- [30] A.J. Stone, D.J. Wales, Theoretical studies of icosahedral C60 and some related species, *Chem. Phys. Lett.* 128 (1986) 501–503.
- [31] K. Takei, N. Terada, K. Kumai, T. Iwahori, T. Uwai, T. Miura, Effects of the macroscopic structure of carbon black on its behaviour as the anode in a lithium secondary cell, *J. Power Sources* 55 (1995) 191–195.